Tina Memo No. 2005-012

Submitted to Radiology 2005.

Comparison of Cerebral Blood Volume Maps gerenated from T2* and T1-weighted MRI Data in Intra-Axial Cerbral Tumours.

H. A. Harooon, T. F. Pantakar, N. A. Thacker M. L. J. Scott, K. Embleton, X. P. Zhu, K. L. Li and A. Jackson.

Last updated
5 / 9 / 2005

Imaging Science and Biomedical Engineering Division,
Medical School, University of Manchester,
Stopford Building, Oxford Road,
Manchester, M13 9PT.

Comparison of Cerebral Blood Volume Maps generated from T_2*- and T_1-weighted MRI Data in Intra-Axial Cerebral Tumours

Type of Manuscript: ORIGINAL RESEARCH

ABSTRACT

Purpose: To compare parametric maps, measured values and value distributions of cerebral blood volume (CBV) derived from 1) first pass T_1-weighted dynamic contrast-enhanced (DCE) data (T_1-CBV) and 2) T_2*-weighted DCE data (T_2*-CBV) in patients with intraaxial tumours. *Materials and Methods*: Sequential T_1- and T_2*-weighted DCE-MRI acquisitions were performed in 9 patients with cerebral neoplasms. CBV maps were calculated from T_2*-weighted data using a conventional curve fitting technique and from T_1-weighted first pass data using the recently described leakage profile model. Regions of interest were manually drawn around enhancing tumour tissue on matched slices and median tumour values and conspicuity indexes of CBV from the two techniques were compared. Pixel-by-pixel scattergrams of values in normal brain in a representative matched slice were produced for each case. 3D correlation renderings from both DCE-MRI datasets of a representative case were also produced for visual comparison. *Results:* Distortion of blood vessels and around susceptibility interfaces was evident on T_2*-CBV but not on T_1-CBV maps. Median ROI T_1- and T_2*-CBV measurements showed good correlation ($r=0.667, p<0.05$) in enhancing tumour, and there was no significant difference in conspicuity. Pixel-by-pixel comparison showed excellent correlation within normal brain ($r=0.96, p<0.001$). 3D renderings from T_1-weighted data were visually superior. *Conclusion:* Leakage-free T_1-CBV maps correlate well with conventionally generated T_2*-CBV maps, both in terms of median measurements from tumour tissue and visual distribution of blood vessels. T_1-CBV maps do not suffer from the susceptibility artefacts seen in T_2*-CBV maps and offer higher through plane spatial resolution.

Index Terms: Brain neoplasms, MR; Cerebral blood vessels, anatomy; Magnetic Resonance (MR), perfusion study; Magnetic Resonance (MR), guidance; Magnetic Resonance (MR), treatment planning

INTRODUCTION

The development of new blood vessels in tumours depends on the process of angiogenesis. Under ischemic and hypoglycaemic challenge developing tumour cells produce cytokines and other vascular mediators which cause sprouting of endothelial cells from local blood vessels and a number of other physiological and developmental changes (1, 2). These lead to the in-growth of new blood vessels and vascularisation of the tumour. In general terms more aggressive, rapidly growing tumours will provide a stronger angiogenic stimulus and are characterised by increased microvascular density (MVD) on histological examination. A clear relationship between microvascular density and prognosis has been demonstrated for many tumour types which encouraged the development of non-invasive imaging based techniques that try to duplicate these measurements *in vivo* (3-5). The best documented of these is the measurement of regional cerebral blood volume (CBV) using dynamic contrast enhanced MRI. Several groups have demonstrated a clear relationship between CBV and histological grade in cerebral glioma and in a number of other tumour types (6-16). Areas of increased CBV within the enhancing components of gliomas correspond well with areas of increased fluorodeoxyglucose uptake on PET and with histological evidence of tumoral de-differentiation (17). As a result CBV maps are increasingly used in clinical assessment of patients with intracerebral tumours and appear to have application in tumour diagnosis, classification and particularly for the targeting of stereotactic surgical biopsy and post resection radiotherapy (18-22).

The most commonly applied method for mapping CBV is based on dynamic contrast enhanced imaging using susceptibility (T_2*) weighted images (DSCE-MRI) (19, 23, 24). This approach was first used to study the perfusion of normal cerebral capillary beds in grey

and white matter where the blood brain barrier (BBB) is intact and gadolinium based contrast agents can be assumed to act as purely intravascular markers. In these applications susceptibility based contrast mechanisms have the advantage over other MR techniques of increased signal to noise ratio in areas of low blood volume such as capillary beds. However susceptibility based techniques have significant disadvantages related to spatial distortion occurring in areas of paramagnetic variation and residual relaxivity effects in areas of extravascular contrast leakage. This has led several workers to try to derive CBV maps from T_1 weighted data (25-29). Although these methods showed some promise they are not routinely used, largely because of their tendency to give rise to erroneously high estimates of CBV in areas of extravascular contrast leakage.

In 2000, Li et al. (17, 30, 31) described a novel method for the analysis of relaxivity (T_1) based dynamic contrast enhanced MRI (DRCE-MRI) which uses a shape-based analysis to decompose the dynamic contrast concentration time course data into intra- and extra-vascular components. One consequence of this analytical approach is the generation of an estimate of the intravascular contrast concentration time course curve that is free of leakage effects and therefore ideal for the calculation of leakage-free estimates of CBV. Examination of the method using Monte Carlo simulation techniques has shown that the representation of CBV values can be expected to be accurate across a wide range of CBV values (30).

The purpose of the study presented here is to compare this novel DRCE-MRI technique with conventional DSCE-MRI approaches. The CBV maps generated from both methods have been compared in terms of image quality (spatial information, distortions, etc.), pixel value distributions within normal brain and measured values within intraaxial cerebral tumours.

The aim is to determine the suitability of these CBV maps for diagnosis, grading and the planning and guidance of procedures such as surgery and radiotherapy.

MATERIALS AND METHODS

Nine patients (4 females and 5 males; mean age 48.2 years) with intra-axial cerebral neoplasms (see Table 1) were recruited into the study. All patients gave informed consent and the Central Manchester Healthcare NHS Trust and Salford Royal Hospitals NHS Trust medical ethical committees approved the protocols.

Image Acquisition

Imaging was performed on a 1.5 tesla MR system (Philips Medical Systems, Best, The Netherlands) using a birdcage head-coil.

Routine clinical T_1- and T_2-weighted anatomical imaging was performed in all patients prior to dynamic studies. Post-contrast T_1-weighted volume images (TR 24 ms / TE 11 ms) were acquired at the end of the dynamic studies and used for qualitative comparison with parametric maps of CBV.

For acquisition of T_1-weighted dynamic contrast-enhanced data, a 3D T_1-FFE (T_1 fast field echo) scanning sequence was applied, with an image matrix of 128 × 128 pixels and 25 slices in the axial plane. The field of view used was 230 mm (square), with a slice thickness of 6 mm with 3 mm overlap (Fourier interpolation), resulting in an effective slice thickness of 3 mm. TR was set at 4.2 ms, and TE at 1.2 ms. Three pre-contrast data sets were acquired for the baseline T_1 calculation using flip angles of 2°, 10° and 35°. This was followed by a dynamic contrast-enhanced acquisition series at a flip angle of 35°, consisting of 120 scans with a temporal spacing of approximately 5 seconds. Gadolinium-based contrast agent (Gd-

DTPA-BMA; Omniscan™, Amersham Health AS, Oslo, Norway) was injected as a bolus over 4 seconds at a dose of 0.1 mmol/kg of body weight.

Acquisition of T_2*-weighted data was carried out immediately after completion of T_1-weighted data acquisition so that pre-enhancement would minimize residual relaxivity effects ('T_1 shine through') in the dynamic data (32). T_2*-weighted (T_2*W) dynamic contrast-enhanced data was acquired using a multislice 2D T_2*W-FEEPI (field echo EPI) sequence. The image matrix was 128 × 128 pixels, with 9 slices in the axial plane. The field of view was again 230 mm (square), with slice thickness of 5 mm with 1 mm interslice gap, giving an effective slice thickness of 6 mm. TR was set at 440 ms, and TE at 30 ms. The dynamic contrast-enhanced series consisted of 52 scans at a flip angle of 35° and a temporal spacing of 1.8 s. A second dose of contrast agent (Gd-DTPA) was injected after the fifth dynamic scan using the same protocol described above.

For all scans the tumour was centred in the imaging volume, the imaging volume included the superior sagittal sinus to provide a vascular input function for analysis and the geometry of the T_2*W acquisitions was selected from the preceding T_1W acquisition so that images were spatially coincident with the central images in the T_1W dynamic dataset.

Image Analysis

Dynamic contrast-enhanced T_1-weighted data was analysed using the First Pass Leakage Profile (FPLP) method described by Li et al (17, 31). This technique uses a shape analysis to decompose contrast concentration time course data into two separate components representing intra- and extra-vascular contrast agent, allowing calculation of CBV free from the effects of

contrast leakage (T_1-CBV), and of the transfer coefficient (K_{fp}) for the passage of contrast between the plasma and the extracellular extravascular space (EES).

T_2*-weighted dynamic contrast-enhanced data was analysed using the technique described by Zhu et al. (10), based on the techniques of Kassner et al. (32). Multi-slice maps of rate of change of T_2* (ΔR_2*) were calculated from the T_2*W-FEEPI dynamic data signals for each dynamic phase and a gamma variate model (33) was used to fit the first pass ΔR_2*(t) data. Relative cerebral blood volume (rCBV) maps were calculated by pixel-by-pixel integration of the resulting gamma variate curves.

Comparison of T_1-CBV and T_2-CBV*

Visual comparison was performed between maps of T_1-CBV, T_2*-CBV and standard post-contrast T_1W anatomical images. Qualitative analysis included calculation of lesion conspicuity, a calculation of the correlation coefficient between median CBV values from each technique and an attempt to produce pixel by pixel correlation values from one representative case.

Due to spatial distortions resulting from susceptibility effects in the T_2*-weighted acquisition it was not possible to reliably apply automated coregistration of T_1W and T_2*W images. Separate corresponding regions of interest (ROIs) were therefore manually defined on matched T_1W and T_2*W images. ROIs were drawn by an experienced neuroradiologist (TAP) and were defined on contrast enhanced images from the late phase dynamic acquisitions. ROI definition included all enhancing components of the tumour but excluded areas of non-enhancement. Calculated values of CBV from T_2* weighted images were

normalized to a value of 1 for a group of voxels (to avoid noise) with an intensity value of greater than 99% of the maximum (assumed to be 100% CBV) to obtain an estimate of absolute CBV. Median tumour CBV values from T_1-CBV and T_2*-CBV were calculated from each ROI, the values were plotted on a scattergram and the correlation between the values tested using Pearson's correlation coefficient. In addition direct visual comparison of T_1-CBV and T_2*-CBV maps was performed using a standardized colour map to aid comparison.

ROIs were also drawn on normal appearing white matter on both T_1-CBV and T_2*-CBV maps, and the mean (μ) and standard deviation (σ) from these were compared to values from the enhancing tumour ROIs in the same maps, to ascertain an index of tumour conspicuity using the following expression:

$$\text{conspicuity} = \frac{\left|\mu_{tumour} - \mu_{white\_matter}\right|}{\sigma_{tumour} + \sigma_{white\_matter}}$$

Since distortion on T_2*W images prevents accurate coregistration with T_1W images we compared pixel-by-pixel values of T_1-CBV and T_2*-CBV in non-tumour brain using the following method.

A single corresponding slice was chosen from the T_1-CBV and T_2*-CBV maps of a representative case and manually registered. The T_1-CBV map was then normalised to the T_2*-CBV by finding the peak in the distribution of the logged CBV ratio over all voxels. Actually, scattergrams were produced of the square-root of the CBV estimates from normal vascularised brain only in the two data sets over a range of 0 – 0.6 in square-root CBV ($\sqrt{\text{CBV}}$). The square root is taken for two reasons: first it produces voxel CBV estimates which have uniform error, and secondly, it expands the dynamic range of the data making it

easier to see trends in the correlation between the two datasets. A second scattergram was obtained by taking the most similar value from the T_1-CBV image to the T_2*-CBV image corresponding to a half pixel linear interpolation in one of four directions (anterior, posterior, left, right) – a *pixel shuffle* technique. This is intended to account for slight non-rigidity between the two volumetric acquisitions and broadening of large blood vessels in T_2* data due to susceptibility effects.

Finally, a direct qualitative comparison was made between volume rendered datasets from each technique. Due to the high level of noise in parametric calculated images, volume rendering was based on specifically calculated correlation images for each dataset. Signal intensity time courses were extracted for both a major vessel and enhancing tumour. These time courses were correlated with the time course from each individual voxel within the original volume, resulting in two sets of volume data with a dynamic range of -1 to +1 representing the correlation coefficients. These volumes of correlation coefficients were rendered using Amira™ (TGS Template Graphics Software, Inc., USA). The quality of the individual volume renders from DSCE-MRI and DRCE-MRI were compared using a four point scale (0: non-diagnostic; 1: poor; 2: satisfactory; 3: excellent), evaluated by experienced neuroradiologists (AJ and TAP).

RESULTS

Parametric images from all patients were of good quality without motion artefacts. There was no evidence of residual relaxivity effects ('T_1 shine through') in the dynamic T_2*-weighted data, which was tested as described previously (32).

Figure 1 shows a typical representative axial slice through the centre of a high grade glioma (patient 8). A standard high resolution T_1-weighted volume post-contrast anatomical image showing the enhancing portion of the tumour and enhanced vasculature (Fig. 1(a)) is provided for comparison with parametric maps. Fig. 1(b) is a T_2*-CBV map at the same location as that of Fig. 1(a) and displays the distribution of CBV values within the brain and tumour tissue (note that the skull and scalp have been stripped from this image during processing). Normal vasculature, such as the branches of the middle cerebral artery and the cerebral veins, show high values of CBV as expected, and the enhancing portion of the tumour shows a heterogeneous distribution of CBV values. There is good differentiation of normal grey and white matter. Note that blood vessels appear much broader and smoother-edged on the T_2*-CBV map than on the high resolution anatomical image. There is also considerable signal drop-out and distortion in the basal prefrontal cortex due to susceptibility artefact resulting from air in the paranasal sinuses. Fig. 1(d) is a T_1-CBV map at the same location as Fig. 1(a). In contrast to Fig. 1(b) the map shows improved demonstration of high spatial frequency features and anatomical details, particularly vascular structure, corresponding closely to the anatomical image (Fig. 1(a)). The signal-to-noise ratio in normal grey and white matter in Fig. 1(d) is poorer than in the T_2*-CBV image but still allows clear subjective visual discrimination. The spatial distribution of CBV values in Fig. 1(b) and 1(d) is similar in normal brain, tumour and vessels. The FPLP method also generates maps of K_{fp} as shown in

Fig. 1(c) indicating an intact blood brain barrier where K_{fp} is zero or consistent with noise, and areas of higher K_{fp} representing contrast leakage only within the tumour and choroid plexus.

Figures 2(a) and 2(b) are T_1-CBV and T_2*-CBV maps of the tumour and major basal arteries in patient 1. These images have been chosen to show the extent of the broadening of major blood vessels in the T_2*-CBV map compared with the same vessels in the T_1-CBV map and in the high resolution anatomy image (Fig. 2(c)), and have been windowed accordingly. Marked distortion and broadening of the main blood vessels in the T_2*-CBV image is clearly observed, and some detail of vascular structure is obscured in comparison to the T_1-CBV map. When compared to the high resolution anatomy image the large vessels seen in the T_1-CBV map correspond closely to their true location and size.

Figure 3 shows a plot of median measurements from the tumour ROIs on T_2*-CBV and spatially corresponding T_1-CBV maps. There is a significant correlation between these median values of T_1-CBV and T_2*-CBV ($r = 0.667$, $p = 0.05$). Comparison of tumour conspicuity values between T_1-CBV and T_2*-CBV maps showed no significant difference; hence visual identification of tumour tissue is equally good on both. The scatter plot in Figure 4 shows the pixel by pixel variation between T_1-CBV and T_2*-CBV in normal brain. The plot illustrates a strong correlation between CBV estimates from the two techniques ($r = 0.92$, $p < 0.001$) and three additional features. First, estimates of T_1-CBV extend down to zero, whereas those from T_2*-CBV appear to be restricted to values above 0.01 CBV (0.1 in square-root CBV). This is entirely consistent with the expected susceptibility effects of enhancing capillary beds in T_2* images. Secondly, the correlation is strong but with a broad random component. Thirdly, there is some evidence for an excess of large (> 0.2 CBV)

values in T_2*. Figure 5 is a pixel-by-pixel scattergram representing the same data using the pixel shuffle technique, which is intended to reduce differences due to small local spatial distortions. The results indicate that both approaches to CBV estimation are consistent ($r = 0.96$, $p < 0.001$) with the exception of spatial distortion effects in T_2*-CBV, the differences being due to capillary enhancement occurring only in CBV values below those generally common in brain tissue.

3D volume renderings from DRCE-MRI and DSCE-MRI data are shown in Figure 6. Corresponding rendered mappings of correlation with an enhancing portion of tumour tissue (Fig. 6(a)) and with a major blood vessel (Fig. 6(b)) from DRCE-MRI data demonstrate high quality volumetric information about the location of the tumour and major vasculature in relation to the patient's head (the skull, scalp, ears and nose are clearly visible). Fig. 6(a) essentially gives an indication of voxels having enhancement time courses consistent with contrast leakiness, and Fig. 6(b) of voxels having enhancement time courses consistent with a major blood vessel. The low signal-to-noise ratio of normal grey and white matter vasculature in the T_1-weighted data aids the clear visualisation of tumour and major vasculature within the volume. Only the mapping of correlation with a major blood vessel for the DSCE-MRI data is shown in Fig. 6(c) because the correlation mapping with enhancing tumour was very similar. The absence of the skull and scalp make it difficult to perceive the relationship between the brain and anatomy. The broadening of normal grey and white matter vasculature is visible. Major vasculature and the tumour margins are not easily distinguishable in the rendered volume, being obscured by the vessels of the brain parenchyma. Mean visual quality scores for renderings from T_1- and T_2*-weighted data were 2.6 and 1.2 respectively.

DISCUSSION

Measurements of CBV based on DSCE-MRI techniques have clinical significance in a range of disease states and appear to provide similar information to fluorodeoxyglucose PET scanning concerning the presence and distribution of tumour tissue heterogeneity (34). In patients with stroke, regional changes in CBV correlate poorly with local flow changes and far better with changes in local water diffusion characteristics and appear to reflect local autoregulatory status (35, 36).

The generation of quantitative CBV maps has traditionally been based on T_2* weighted sequences utilizing susceptibility contrast mechanisms. DSCE-MRI approaches were initially used because the susceptibility contrast mechanism gives a superior signal-to-noise ratio in low density capillary beds such as are seen in normal brain (23, 37, 38). In addition, the signal changes seen on T_2* weighted images in normal brain are less affected by contrast in large vessels, so that DSCE-MRI acquisitions were classically considered as "capillary weighted". These properties can be considered beneficial for the study of normal brain tissue where the CBV is low and the blood brain barrier is intact.

However, the use of DSCE-MRI techniques to measure CBV in cerebral tumours is associated with a number of inherent disadvantages. High sensitivity to susceptibility effects is associated with distortions around susceptibility interfaces, which will include the air in the paranasal sinuses and petrous bone and structures containing a high concentration of contrast in enhanced images. Secondly, leakage of contrast due to blood brain barrier breakdown, which is an intrinsic feature of malignant cerebral tumours, will cause competing relaxivity effects on the observed signal changes which will lead to erroneous underestimation of CBV.

In practice, these effects are compensated by decreasing the T_1 sensitivity of the sequences or by contrast pre-enhancement to saturate T_1 based signal change effects as was performed in the current study (32). Thirdly, T_2* weighted images rely on the use of long echo times (TE) to maintain their T_2 sensitivity which reduces the size of the sampling matrix and number of slices which can be acquired within the required temporal resolution (approximately 2 seconds). This can be tackled by the use of echo planar imaging (EPI) acquisitions which greatly enhance acquisition speed but which will impose additional and unpredictable spatial distortions into the image making them potentially unsuitable for spatially-sensitive procedures such as surgical planning applications. These effects can be reduced to some extent by the use of segmented EPI acquisitions and temporal resolution can be maintained by the use of echo shifting techniques in sequences such as PRESTO which also uses a volume acquisition to maintain signal to noise ratio (39).

In view of the problems associated with DSCE-MRI techniques several groups have attempted to use relaxivity based dynamic images (DRCE-MRI) to derive estimates of CBV. The potential advantages of this approach include the lack of spatial distortion associated with T_1W images and the potential for fast 3D imaging approaches without the need for EPI collections. The major problem with DRCE-MRI in enhancing tissues is the inability to separate the effects of intravascular and extravasated contrast on the observed signal change. This means that signal changes in areas of high capillary permeability will result to a large degree from contrast leakage and estimates of CBV will therefore be erroneously high.

Despite this disadvantage, Hacklander's group in the late nineties described the use of DRCE-MRI in cerebral tumours in a series of publications (25-28). This group dealt with the leakage problem by assuming that contrast leakage is so slow that it can be ignored over the time

course of a single passage of a contrast bolus. They stated that: "gadopentate dimeglumine can almost be regarded to be an intravascular contrast agent, even in cases of a disturbed blood brain barrier". They concluded that T_1-CBV measurements could be used in enhancing tissues. However, it is interesting to note that they were unable to demonstrate significant differences between grade III and grade IV glioma even though this has been shown by several groups using susceptibility based techniques (10, 11, 29). In addition, careful comparison of the results from the T_2* and T_1 based techniques shows systematic overestimation of T_1-CBV in tumours with high values (Figure 7 in (28)). Although the authors do not comment on this a similar observation was highlighted by Bruening et al. (29), who described areas of apparently very high CBV on T_1-CBV maps which were not seen on T_2*-CBV. They commented: "In the high grade group, different values between T_1 and T_2 CBV maps were apparent", concluding: "Theoretically one would anticipate that in settings of blood brain barrier disruption there would be a tendency for T_1 rCBV maps to cause elevated rCBV measurements. In contrast T_2 rCBV maps tend to underestimate the apparent rCBV values in the presence of a blood brain barrier breakdown and may show false negative findings in the event of an active tumour recurrence."

In practice, as described above, the tendency for T_2*-CBV maps to underestimate CBV in areas of contrast leakage can be minimised by a variety of acquisition strategies which are discussed in detail by Kassner et al. (32), so that the major residual disadvantages of T_2* based methods are the distortion associated with susceptibility effects and the restrictions on imaging time. The sequences used here represent a compromise between spatial resolution and susceptibility sensitivity using a segmented EPI acquisition protocol to reduce scan time whilst minimising the degree of spatial distortion. Despite this we were only able to collect 9 slices of data at a matrix of 128^2 within the 1.8-second time resolution required and the

resultant images show significant distortions both at tissue-air interfaces and more importantly, around large vessels. Further improvements in gradient performance mean that our current system can collect 12 slices within the same time window but, in reality, the use of T_2* EPI sequences is problematic. The use of optimized T_2* based sequences such as PRESTO offer the opportunity to improve on this performance by combining echo shifted, segmented EPI collection and volume acquisition techniques in order to maximize temporal and spatial resolution whilst limiting sensitivity to susceptibility artefacts and distortions. Although these sequences are still not widely available and we have not used them in this study our experience with them indicates that the improvements in susceptibility distortion are relatively limited and spatial distortion remains a significant problem (32, 40).

The use of DRCE-MRI offers significant theoretical advantages allowing increased sampling speed and therefore greater spatial resolution and coverage. More importantly there is no susceptibility spatial distortion associated with standard T_1W sequences. A third potential advantage is the ability to use reduced contrast doses compared to DSCE-MRI although we have not explored that aspect in this study (28, 29). The major problem with DRCE-MRI is that the signal changes resulting from intravascular contrast and from extravasated contrast occur in the same direction and, since they result from the same physical contrast mechanism, cannot be separated by modifications of the acquisition technique. We have used the first pass leakage profile model described by Li et al. (31, 41) to separate these effects and to generate leakage free T_1-CBV maps. This analysis technique decomposes the contrast concentration time course data from DRCE-MRI into two components: the first due to intravascular contrast agent, and the second due to contrast agent leakage into the extravascular extracellular space. The technique works by using a constrained shape model of each component and decomposing the data to produce the optimised fit to these constraints.

Although the technique was designed to produce estimates of transendothelial contrast transfer coefficient (K^{trans} (42), or more specifically K_{fp} (43)) which are free of intravascular contrast effects it also allows calculation of leakage-free CBV maps. The theoretical advantages in terms of temporal resolution, tissue coverage and freedom from image distortion have been the subject of the present study. However, it is equally important to know that CBV estimates from DRCE-MRI provide comparable biological information to those derived from conventional DSCE-MRI techniques. This study has confirmed that this is the case with close correlation between median values and also excellent pixel-by-pixel agreement, particularly when spatial distortion effects are reduced. The advantages of T_1 techniques allow confident use of parametric maps for image guided surgical procedures and radiotherapy planning without any risk of error due to spatial distortion. The ability to increase coverage and through plane resolution also allows direct 3D visualisation of these data sets with better practical quality than with DSCE-MRI.

In conclusion we would recommend the routine use of T_1-weighted DCE-MRI for the measurement of CBV in cerebral tumours. The technique allows larger sampling volumes, removes the risk of significant spatial distortion, provides biologically equivalent data to conventional T_2*-weighted DCE-MRI methods and has the added advantage of providing high-quality maps of the transfer coefficient.

REFERENCES

1. Shweiki D, Neeman M, Itin A, Keshet E. Induction of vascular endothelial growth factor expression by hypoxia and by glucose deficiency in multicell spheroids: implications for tumor angiogenesis. Proc Natl Acad Sci U S A 1995; 92:768-772.
2. Folkman J. What is the evidence that tumours are angiogenesis dependent? JCNI 1990; 82:4-6.
3. Plate KH, Risau W. Angiogenesis in malignant gliomas. Glia 1995; 15:339-347.
4. Brasch R, Turetschek K. MRI characterization of tumors and grading angiogenesis using macromolecular contrast media: status report. Eur J Radiol 2000; 34:148-155.
5. Padhani AR. Dynamic contrast-enhanced MRI in clinical oncology: current status and future directions. J Magn Reson Imaging 2002; 16:407-422.
6. Sugahara T, Korogi Y, Shigematsu Y, et al. Value of dynamic susceptibility contrast magnetic resonance imaging in the evaluation of intracranial tumors. Top Magn Reson Imaging 1999; 10:114-124.
7. Cha S, Knopp EA, Johnson G, Wetzel SG, Litt AW, Zagzag D. Intracranial mass lesions: dynamic contrast-enhanced susceptibility-weighted echo-planar perfusion MR imaging. Radiology 2002; 223:11-29.
8. Cha S, Pierce S, Knopp EA, et al. Dynamic contrast-enhanced T2*-weighted MR imaging of tumefactive demyelinating lesions. AJNR Am J Neuroradiol 2001; 22:1109-1116.
9. Sugahara T, Korogi Y, Kochi M, Ushio Y, Takahashi M. Perfusion-sensitive MR imaging of gliomas: comparison between gradient-echo and spin-echo echo-planar imaging techniques. AJNR Am J Neuroradiol 2001; 22:1306-1315.

10. Zhu XP, Li KL, Kamaly-Asl ID, et al. Quantification of endothelial permeability, leakage space, and blood volume in brain tumors using combined T1 and T2* contrast-enhanced dynamic MR imaging. J Magn Reson Imaging 2000; 11:575-585.

11. Jackson A, Kassner A, Zhu XP, Li KL. Reproducibility of T2* blood volume and vascular tortuosity maps in cerebral gliomas. J Magn Reson Imaging 2001; 14:510-516.

12. Law M, Yang S, Wang H, et al. Glioma grading: sensitivity, specificity, and predictive values of perfusion MR imaging and proton MR spectroscopic imaging compared with conventional MR imaging. AJNR Am J Neuroradiol 2003; 24:1989-1998.

13. Miyati T, Banno T, Mase M, et al. Dual dynamic contrast-enhanced MR imaging. J Magn Reson Imaging 1997; 7:230-235.

14. Uematsu H, Maeda M, Sadato N, et al. Vascular permeability: quantitative measurement with double-echo dynamic MR imaging--theory and clinical application. Radiology 2000; 214:912-917.

15. Ludemann L, Grieger W, Wurm R, Budzisch M, Hamm B, Zimmer C. Comparison of dynamic contrast-enhanced MRI with WHO tumor grading for gliomas. Eur Radiol 2001; 11:1231-1241.

16. Johnson G, Wetzel S, Cha S, Tofts PS. Simultaneous Measurement of Blood Volume and Vascular Transfer Constant by First Pass Pharmacokinetic Modelling. In:Proceedings of the 10th Scientific Meeting of the ISMRM. Honolulu, Hawai'i, USA, 2002; 2123.

17. Li KL, Zhu XP, Waterton J, Jackson A. Improved 3D quantitative mapping of blood volume and endothelial permeability in brain tumors. J Magn Reson Imaging 2000; 12:347-357.

18. Rosen BR, Belliveau JW, Aronen HJ, et al. Susceptibility contrast imaging of cerebral blood volume: human experience. Magn Reson Med 1991; 22:293-299; discussion 300-293.

19. Aronen HJ, Perkio J. Dynamic susceptibility contrast MRI of gliomas. Neuroimaging Clin N Am 2002; 12:501-523.

20. Maeda M, Itoh S, Kimura H, et al. Tumor vascularity in the brain: evaluation with dynamic susceptibility-contrast MR imaging. Radiology 1993; 189:233-238.

21. Wetzel SG, Cha S, Law M, et al. Preoperative assessment of intracranial tumors with perfusion MR and a volumetric interpolated examination: a comparative study with DSA. AJNR Am J Neuroradiol 2002; 23:1767-1774.

22. Knopp EA, Cha S, Johnson G, et al. Glial neoplasms: dynamic contrast-enhanced T2*-weighted MR imaging. Radiology 1999; 211:791-798.

23. Barbier EL, Lamalle L, Decorps M. Methodology of brain perfusion imaging. J Magn Reson Imaging 2001; 13:496-520.

24. Aronen HJ, Glass J, Pardo FS, et al. Echo-planar MR cerebral blood volume mapping of gliomas. Clinical utility. Acta Radiol 1995; 36:520-528.

25. Hacklander T. Parametric images of cerebral blood volume with T1 FLASH sequences (German). Rontgenpraxis 1995; 48:146-152.

26. Hacklander T, Hofer M, Reichenbach JR, Rascher K, Furst G, Modder U. Cerebral blood volume maps with dynamic contrast-enhanced T1-weighted FLASH imaging: normal values and preliminary clinical results. J Comput Assist Tomogr 1996; 20:532-539.

27. Hacklander T, Reichenbach JR, Hofer M, Modder U. Measurement of cerebral blood volume via the relaxing effect of low-dose gadopentetate dimeglumine during bolus transit. AJNR Am J Neuroradiol 1996; 17:821-830.

28. Hacklander T, Reichenbach JR, Modder U. Comparison of cerebral blood volume measurements using the T1 and T2* methods in normal human brains and brain tumors. J Comput Assist Tomogr 1997; 21:857-866.

29. Bruening R, Kwong KK, Vevea MJ, et al. Echo-planar MR determination of relative cerebral blood volume in human brain tumors: T1 versus T2 weighting. AJNR Am J Neuroradiol 1996; 17:831-840.

30. Li KL, Jackson A. New hybrid technique for accurate and reproducible quantitation of dynamic contrast-enhanced MRI data. Magn Reson Med 2003; 50:1286-1295.

31. Li KL, Zhu XP, Checkley DR, et al. Simultaneous mapping of blood volume and endothelial permeability surface area product in gliomas using iterative analysis of first-pass dynamic contrast enhanced MRI data. Br J Radiol 2003; 76:39-50.

32. Kassner A, Annesley DJ, Zhu XP, et al. Abnormalities of the contrast re-circulation phase in cerebral tumors demonstrated using dynamic susceptibility contrast-enhanced imaging: a possible marker of vascular tortuosity. J Magn Reson Imaging 2000; 11:103-113.

33. Rosen BR, Belliveau JW, Vevea JM, Brady TJ. Perfusion imaging with NMR contrast agents. Magn Reson Med 1990; 14:249-265.

34. Aronen HJ, Pardo FS, Kennedy DN, et al. High microvascular blood volume is associated with high glucose uptake and tumor angiogenesis in human gliomas. Clin Cancer Res 2000; 6:2189-2200.

35. Schaefer PW, Hunter GJ, He J, et al. Predicting cerebral ischemic infarct volume with diffusion and perfusion MR imaging. AJNR Am J Neuroradiol 2002; 23:1785-1794.

36. Kim JH, Lee EJ, Lee SJ, Choi NC, Lim BH, Shin T. Comparative evaluation of cerebral blood volume and cerebral blood flow in acute ischemic stroke by using perfusion-weighted MR imaging and SPECT. Acta Radiol 2002; 43:365-370.

37. Rosen BR, Belliveau JW, Buchbinder BR, et al. Contrast agents and cerebral hemodynamics. Magn Reson Med 1991; 19:285-292.

38. Helenius J, Perkio J, Soinne L, et al. Cerebral Hemodynamics in a Healthy Population Measured by Dynamic Susceptibility Contrast Mr Imaging. Acta Radiol 2003; 44:538-546.

39. Liu G, Sobering G, Duyn J, Moonen CT. A functional MRI technique combining principles of echo-shifting with a train of observations (PRESTO). Magn Reson Med 1993; 30:764-768.

40. Thacker NA, Scott ML, Jackson A. Can dynamic susceptibility contrast magnetic resonance imaging perfusion data be analyzed using a model based on directional flow? J Magn Reson Imaging 2003; 17:241-255.

41. Li K, Jackson A. A new hybrid technique for accurate and reproducible quantitatation of dynamic contrast-enhanced MRI data. MRM 2003; 50:1286-1295.

42. Tofts PS, Brix G, Buckley DL, et al. Estimating kinetic parameters from dynamic contrast-enhanced T(1)-weighted MRI of a diffusable tracer: standardized quantities and symbols. J Magn Reson Imaging 1999; 10:223-232.

43. Haroon HA, Buckley DL, Patankar TA, et al. A comparison of K^{trans} measurements obtained with conventional and first pass pharmacokinetic models in human gliomas. J Magn Reson Imaging 2004; 19:527-536.

TABLES

Table 1: Patient demography.

Patient No.	*Sex*	*Age*	*Histological Grade**
1	M	58	IV
2	M	28	Unconfirmed
3	F	31	II
4	F	22	Unconfirmed
5	F	55	IV
6	M	52	IV
7	F	63	IV
8	M	54	IV
9	M	71	IV

* Grading according to World Health Organisation (WHO) criteria for histopathological findings of tissue biopsy samples, taken after imaging. In general, glioma grade II = fibrillary astrocytoma; III = anaplastic astrocytoma; IV = glioblastoma multiforme. Unconfirmed cases have not had histopathological findings reported.

FIGURE LEGENDS

Figure 1: (**a**) High resolution post-contrast T_1-weighted (volumetric T_1-FFE / TR 24 ms / TE 11 ms) anatomical image showing an enhancing high grade glioma (patient 8). (**b**) Corresponding cerebral blood volume (CBV) map generated from T_2*-weighted EPI dynamic susceptibility-enhanced data (T_2*-CBV) [values range 0 - 100%]. Related maps generated from T_1-weighted fast field echo contrast-enhanced dynamic data of (**c**) K_{fp} [values range 0 – 1.2 min^{-1}] and (**d**) T_1-CBV [values range 0 – 100%]. ((b),(c) and (d) use the same colour rendering table for display.)

Figure 2: Corresponding T_1-CBV (**a**) and a T_2*-CBV (**b**) maps showing a high grade glioma, the circle of Willis and middle cerebral arteries (patient 1). (**c**) High resolution post-contrast T_1-weighted (volumetric T_1-FFE / TR 24 ms / TE 11 ms) anatomical image showing the same location. ((a) and (b) use the same colour rendering table for display.)

Figure 3: Comparison of the median measurement taken from enhancing tumour tissue ROIs on manually matched slices of T_1-CBV maps against T_2*-CBV, for all our tumour cases. (rho = 0.667, $p < 0.05$)

Figure 4: Pixel-by-pixel scattergram of a visually matched brain slice from the T_1-CBV and T_2*-CBV maps in patient 7, using a vascular region of normal brain only. The square-root of the values from the two maps are used to ensure uniform error and to expand the dynamic range of data for visualisation (see text). ($r = 0.92$, $p < 0.001$)

Figure 5: Pixel-by-pixel scattergram generated from the same data as in Fig. 4 except that this has been produced by a pixel shuffling method between CBV maps to allow for spatial distortions in the T_2*-CBV map (see text). ($r = 0.96$, $p < 0.001$)

Figure 6: 3D volume rendered correlation mappings with enhancing portion of tumour tissue (**a**) and with a major blood vessel (**b**) from DRCE-MRI data, and with a major blood vessel from DSCE-MRI data (**c**).

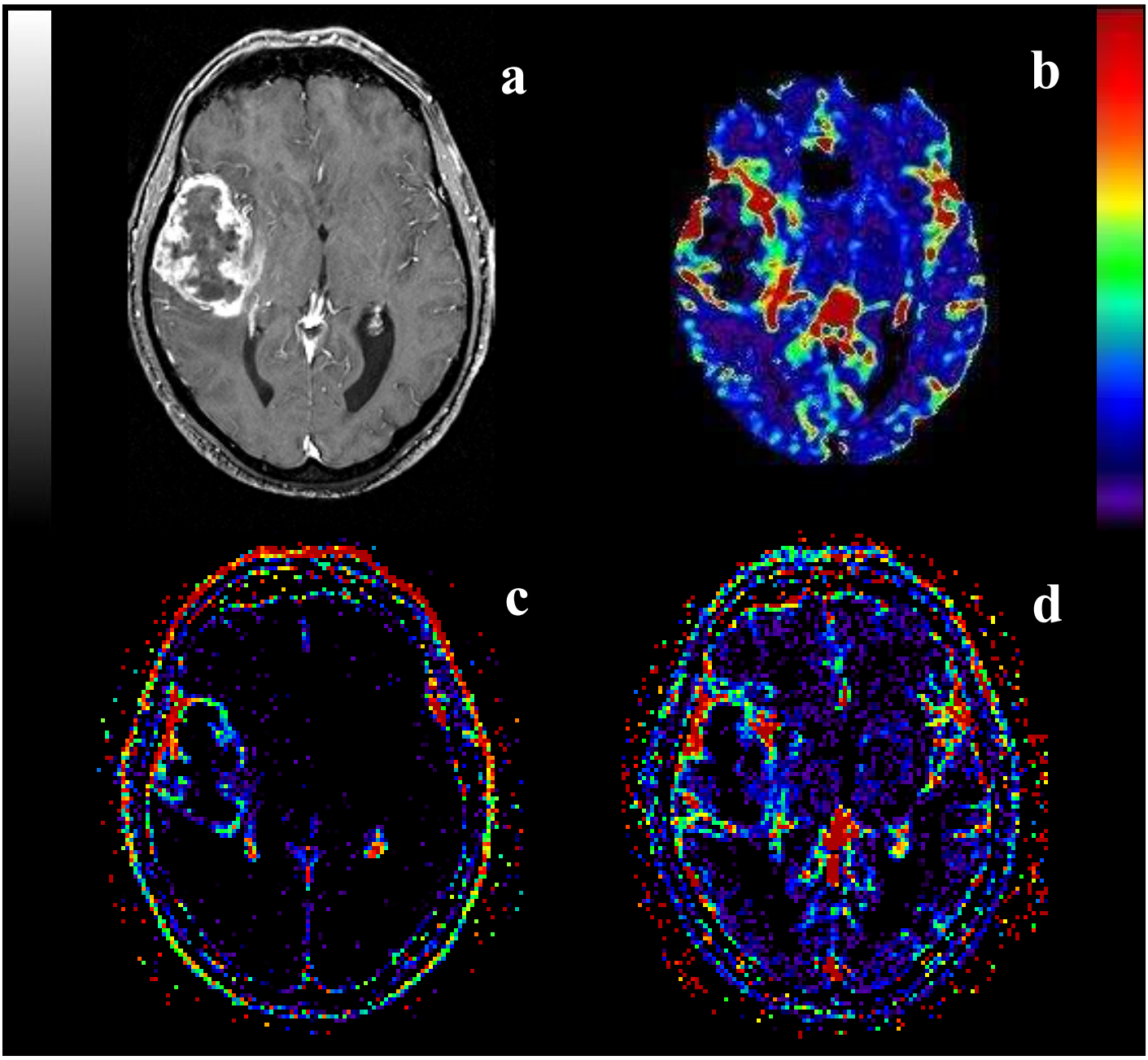

Figure 1: (**a**) High resolution post-contrast T_1-weighted (volumetric T_1-FFE / TR 24 ms / TE 11 ms) anatomical image showing an enhancing high grade glioma (patient 8). (**b**) Corresponding cerebral blood volume (CBV) map generated from T_2*-weighted EPI dynamic susceptibility-enhanced data (T_2*-CBV) [values range 0 - 100%]. Related maps generated from T_1-weighted fast field echo contrast-enhanced dynamic data of (**c**) K_{fp} [values range 0 – 1.2 min^{-1}] and (**d**) T_1-CBV [values range 0 – 100%]. ((b),(c) and (d) use the same colour rendering table for display.)

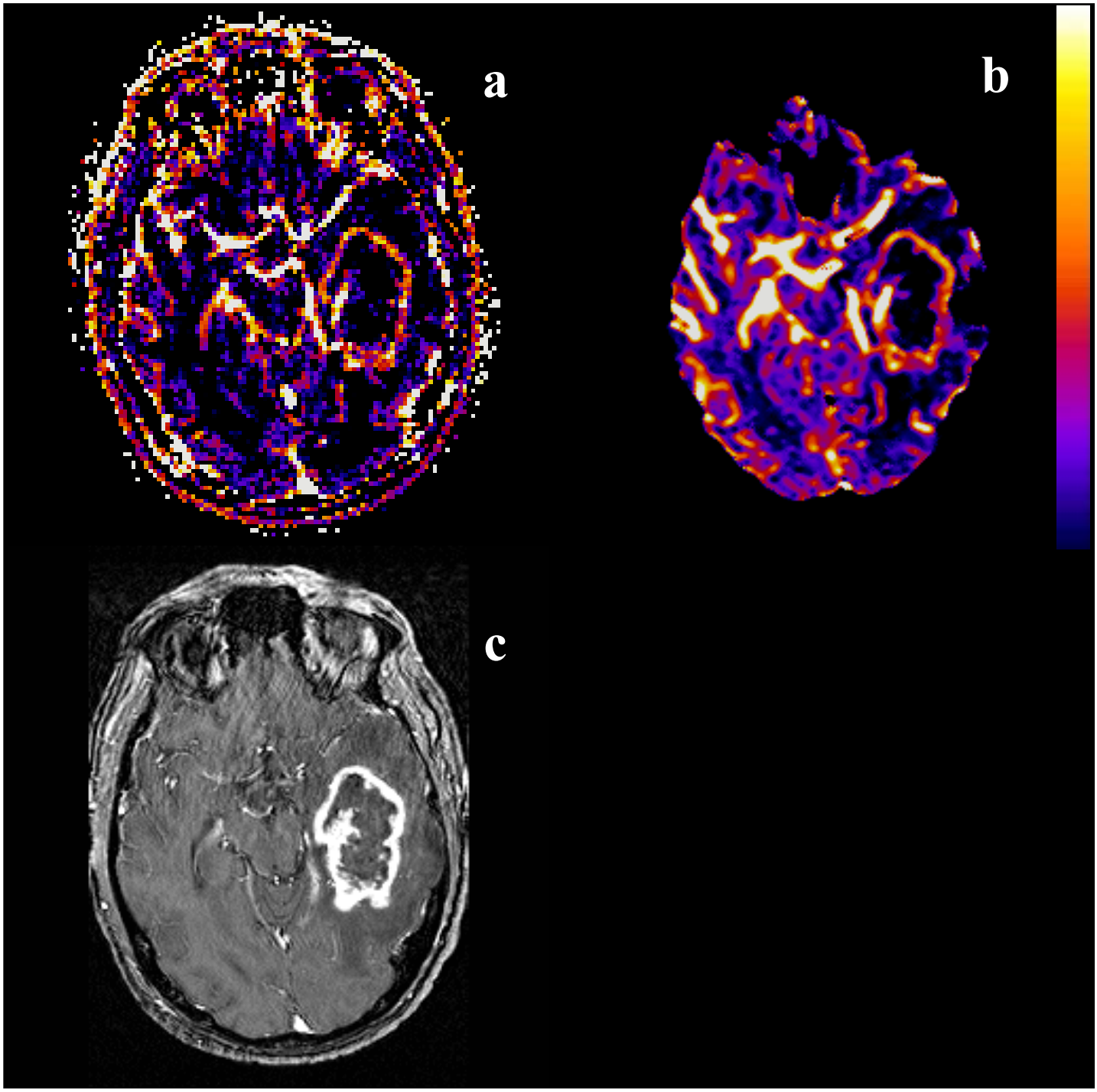

Figure 2: Corresponding T_1-CBV (**a**) and a T_2*-CBV (**b**) maps showing a high grade glioma, the circle of Willis and middle cerebral arteries (patient 1). (**c**) High resolution post-contrast T_1-weighted (volumetric T_1-FFE / TR 24 ms / TE 11 ms) anatomical image showing the same location. ((a) and (b) use the same colour rendering table for display.)

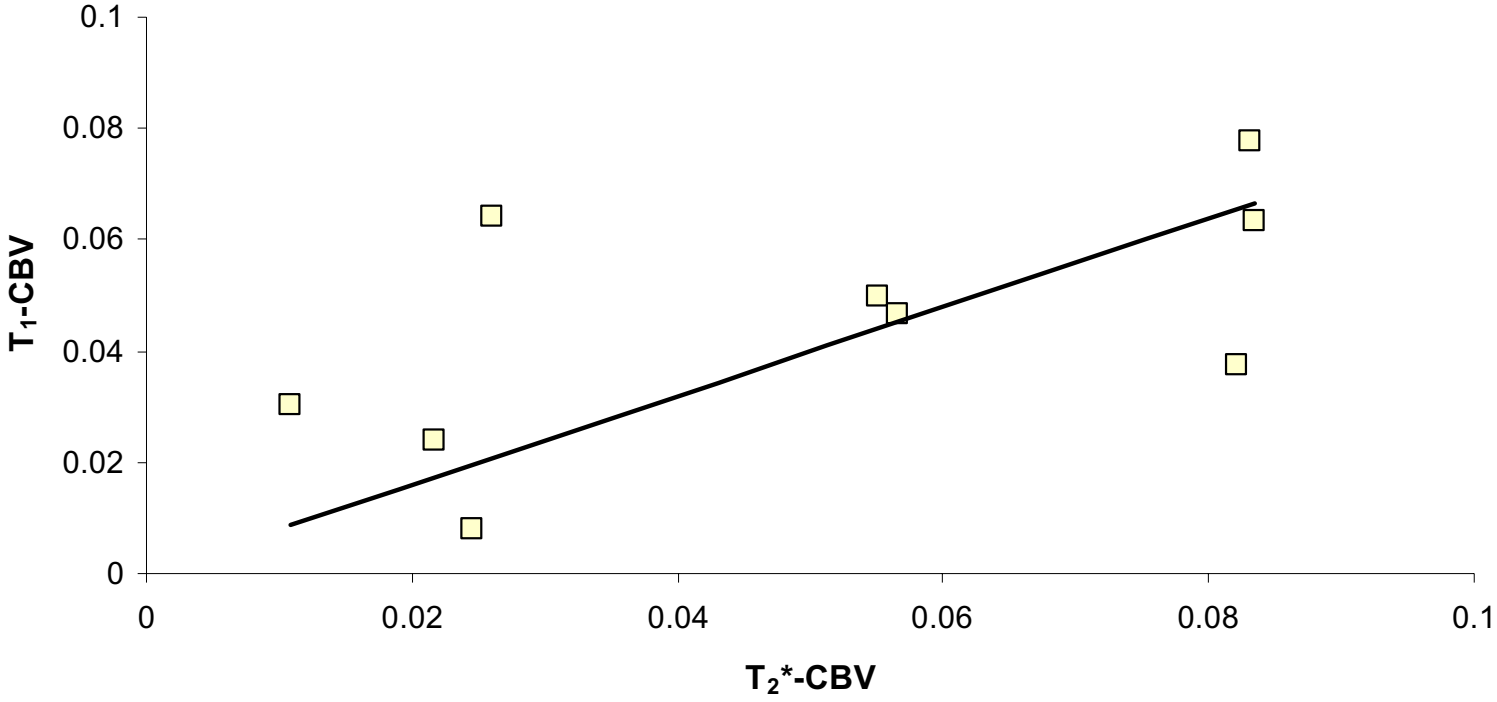

Figure 3: Comparison of the median measurement taken from enhancing tumour tissue ROIs on manually matched slices of T_1-CBV maps against T_2*-CBV, for all our tumour cases. (rho = 0.667, $p < 0.05$)

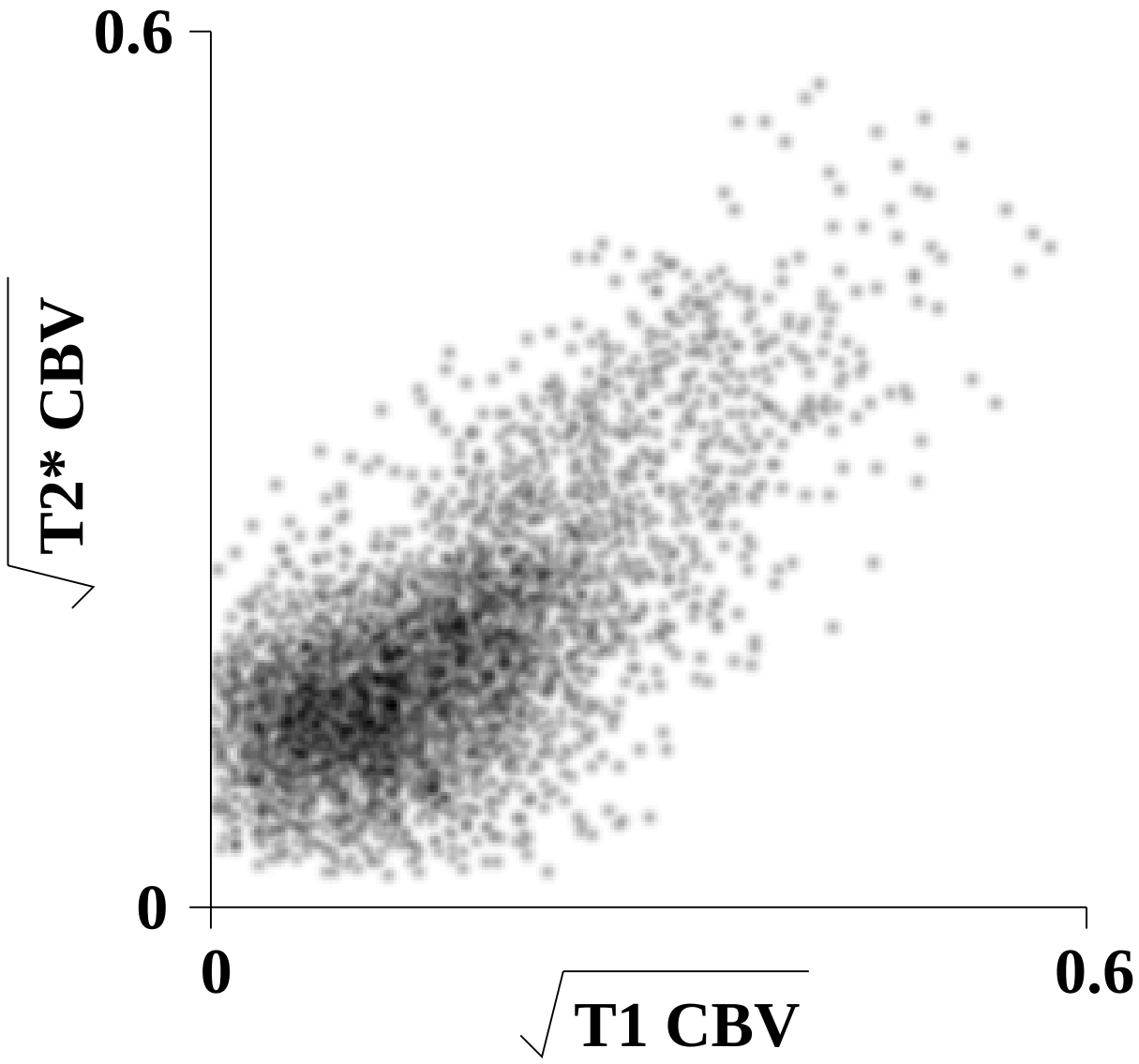

Figure 4: Pixel-by-pixel scattergram of a visually matched brain slice from the T_1-CBV and T_2*-CBV maps in patient 7, using a vascular region of normal brain only. The square-root of the values from the two maps are used to ensure uniform error and to expand the dynamic range of data for visualisation (see text). ($r = 0.92$, $p < 0.001$)

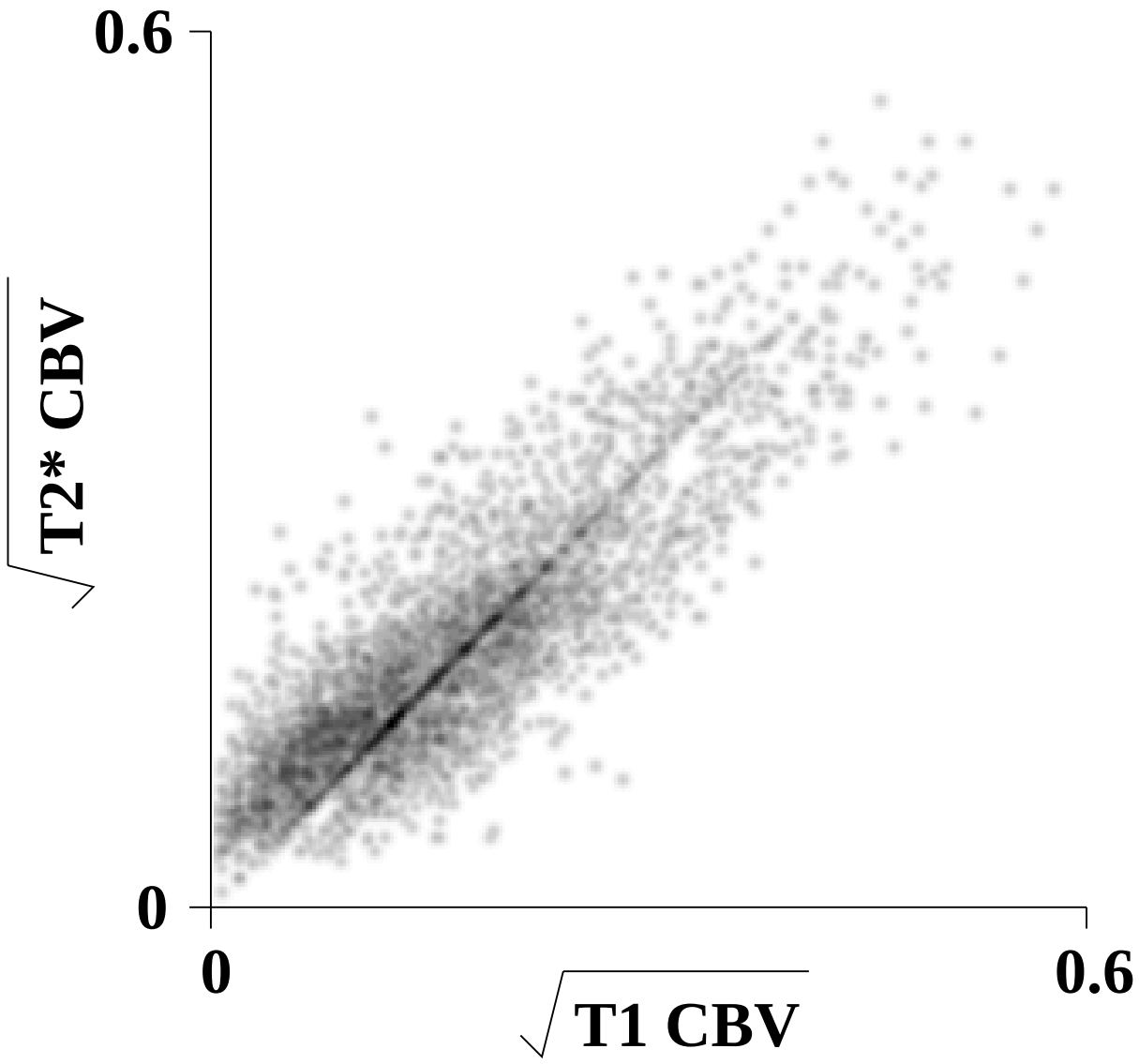

Figure 5: Pixel-by-pixel scattergram generated from the same data as in Fig. 4 except that this has been produced by a pixel shuffling method between CBV maps to allow for spatial distortions in the T_2*-CBV map (see text). ($r = 0.96$, $p < 0.001$)

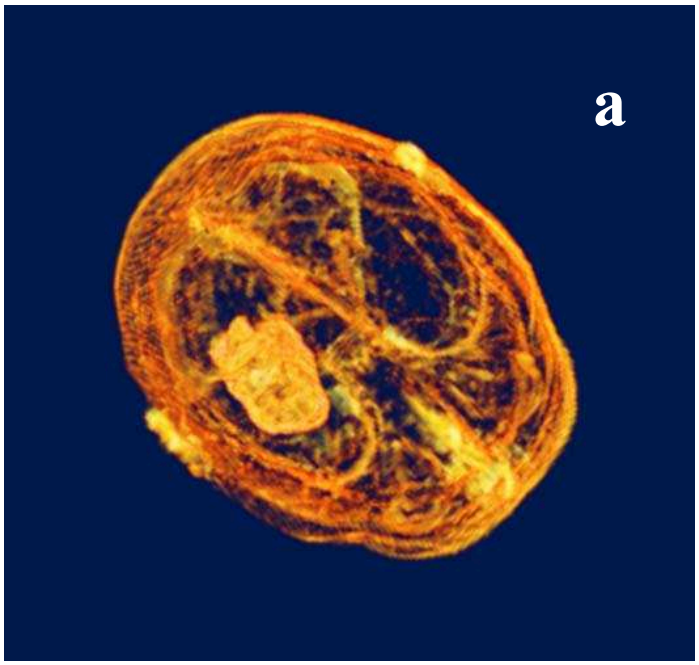

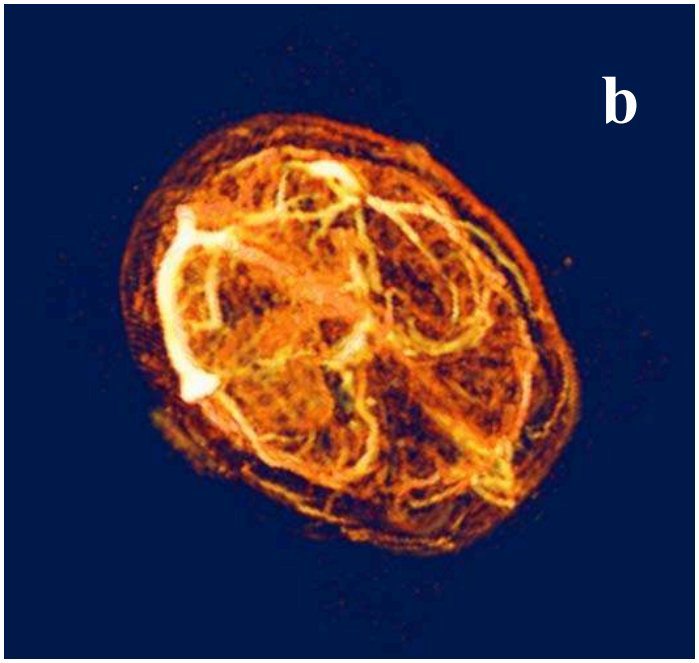

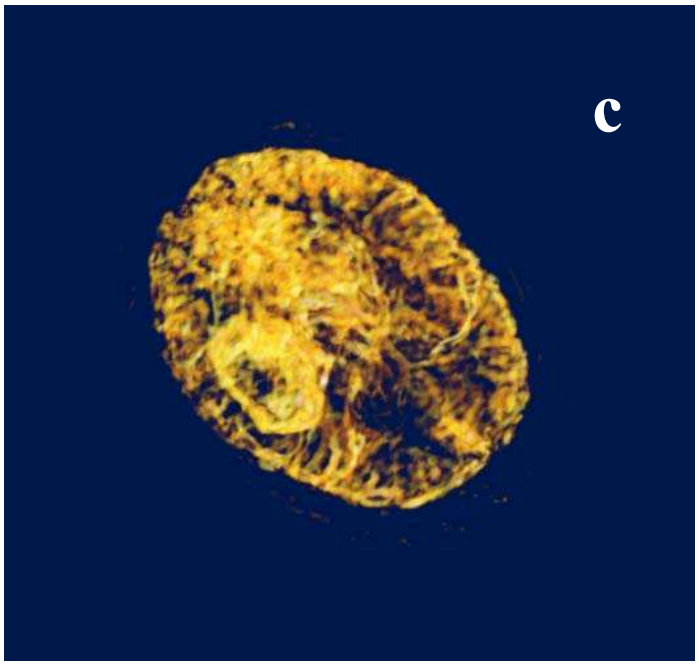

Figure 6: 3D volume rendered correlation mappings with enhancing portion of tumour tissue (**a**) and with a major blood vessel (**b**) from DRCE-MRI data, and with a major blood vessel from DSCE-MRI data (**c**).